

Tuning the magnetic properties of Kitaev materials via the antiferromagnetic proximity effect: Novel phases and application to an α - $\text{RuCl}_3/\text{MnPS}_3$ bilayer

Pedro M. C onsoli,[†] Ezra Day-Roberts,[†] Johannes Knolle,^{‡,¶,§} Antia S. Botana,^{*,†}
and Onur Erten^{*,†}

[†]*Department of Physics, Arizona State University, Tempe, AZ 85287, USA*

[‡]*Munich Center for Quantum Science and Technology (MCQST), Schellingstrasse 4, 80799
Munich, Germany*

[¶]*Technical University of Munich, TUM School of Natural Sciences, Physics Department,
TQM, 85748 Garching, Germany*

[§]*Blackett Laboratory, Imperial College London, London SW7 2AZ, United Kingdom*

E-mail: antia.botana@asu.edu; onur.erten@asu.edu

KEYWORDS: α - RuCl_3 , MnPS_3 , 2D magnetism, quantum spin liquids, antiferromagnetic proximity effect, skyrmion crystals

Abstract

In recent years, the increasing level of control over van der Waals (vdW) heterostructures has opened new routes to tune the properties of quantum materials. Motivated by these developments, we examine the potential consequences of interfacing a Kitaev honeycomb magnet, such as α - RuCl_3 , with a nearly lattice-matched vdW antiferromagnet. By combining perturbation theory, exact diagonalization, and a classical energy-minimization method, we show that an effective staggered magnetic field originating from the vdW antiferromagnet can drive a monolayer of a Kitaev material into various novel phases, including an antichiral Kitaev spin liquid, a nonmagnetic nematic phase, and different types of skyrmion crystals. We then apply first-principle

simulations to assess the prospect of concretely realizing this setup in a heterobilayer of α - RuCl_3 and the easy-axis antiferromagnet MnPS_3 .

A long-standing quest that has united the fields of condensed matter physics and materials chemistry for decades is the search for experimental realizations of quantum spin liquids (QSLs) – elusive states of matter that display fascinating properties such as long-range entanglement, fractionalized excitations, and emergent gauge fields.^{1–4} By now, various classes of Mott insulators have been identified as candidates to host QSLs, including the so-called Kitaev materials.⁵ At low energies, these compounds develop spin-orbit entangled $J_{\text{eff}} = 1/2$ magnetic moments which interact primarily through the bond-dependent Ising exchange couplings observed in Kitaev’s honeycomb model.^{6–8} Yet while the latter is celebrated for harboring an exact QSL ground state, Kitaev materials tend to exhibit long-range magnetic order at low temperatures due to additional magnetic interactions.^{8–13}

In this context, there have been continued efforts to understand whether external perturbations can stabilize proximate QSLs as ground states of Kitaev magnets. Although this strategy has not been conclusively successful so far, it has generated tremendous activity, especially with regard to α - RuCl_3 . In this van der Waals (vdW) material, magnetic Ru^{3+} ions form a honeycomb lattice^{14,15} and antiferromagnetic (AFM) zigzag order emerges below a temperature $T_N \sim 7$ K.^{16–20} However, a moderate in-plane magnetic field suppresses the zigzag phase^{15,16,21} and drives α - RuCl_3 into a disordered intermediate-field regime whose nature remains under debate to this day.^{22–29}

In parallel, various other routes have been explored as means of uncovering new phases in α - RuCl_3 . Apart from chemical substitution, carrier doping,³⁰ strain engineering^{31–34} and twisting,³⁵ an appealing alternative is to interface α - RuCl_3 with a different vdW material. A first example along these lines is provided by α - RuCl_3 /graphene heterostructures, where charge transfer and screening can lead to novel correlated states at the interface.^{36–43} A second example involves α - RuCl_3 / CrX_3 ($X = \text{I, Cl}$) heterostructures, in which the ferromagnetic (FM) order in CrX_3 acts on α - RuCl_3 as a magnetic field with a dominant *uniform* spatial component.⁴⁴

Here, we examine a related setting where a Kitaev material is subject to a *staggered* magnetic field, which may originate from an adjacent vdW material with AFM order. A primary motivation to pursue this route is that Kitaev models with FM and AFM couplings have starkly different responses to external magnetic fields: the AFM model exhibits richer physics in a spatially uniform field, whereas the converse occurs in a staggered field.⁴⁵ Since a significant fraction of Kitaev materials – including α - RuCl_3 and other compounds whose magnetic ions have d^5 or d^7 electronic configurations^{7,8,46,47} – are believed to possess FM Kitaev couplings, it is natural to ask what other phases they might realize in the proposed

AFM proximity environment. We tackle this question by studying the influence of a staggered magnetic field on two-dimensional spin models that interpolate between a pure FM Kitaev model and parameter sets previously proposed for α -RuCl₃. As the model can be potentially realized in practice by interfacing an adjacent vdW material with AFM order, we also perform first-principles simulations in a heterobilayer of α -RuCl₃ and the easy-axis antiferromagnet MnPS₃. We find that when a weak staggered field is applied to a Kitaev spin liquid (KSL), it gives rise to Majorana Fermi surfaces and antichiral edge states.⁴⁸ At higher fields, a nematic phase without long-range magnetic order may emerge. In contrast, when the staggered field is applied to a zigzag phase, it induces a metamagnetic transition into a robust state with triple-**Q** magnetic order. We propose this state is a skyrmion crystal with a net topological charge, and discuss the possibility for it to be realized in an α -RuCl₃/MnPS₃ heterobilayer.

The starting point for our model calculations is an effective Hamiltonian

$$\mathcal{H} = \mathcal{H}_K + g\mathcal{H}_{J\Gamma\Gamma'} + \mathcal{H}_h \quad (1)$$

describing a single honeycomb layer of (pseudo)spin-1/2 moments \mathbf{S}_i in a Kitaev material. Although the model does not include additional degrees of freedom, it will be instructive to refer to the aforementioned setup, in which the Kitaev layer (L_1) is interfaced with a monolayer (L_2) of a vdW magnet whose spins \mathbf{s}_i display collinear Néel order. The three terms in Eq. (1) read:

$$\begin{aligned} \mathcal{H}_K &= K_1 \sum_{\gamma=x,y,z} \sum_{\langle ij \rangle_\gamma} S_i^\gamma S_j^\gamma, \\ \mathcal{H}_{J\Gamma\Gamma'} &= J_1 \sum_{\langle ij \rangle} \mathbf{S}_i \cdot \mathbf{S}_j + J_3 \sum_{\langle\langle ij \rangle\rangle} \mathbf{S}_i \cdot \mathbf{S}_j \\ &\quad + \sum_{\gamma} \sum_{\langle ij \rangle_\gamma} \left[\Gamma_1 \left(S_i^\alpha S_j^\beta + S_i^\beta S_j^\alpha \right) + \Gamma'_1 \left(S_i^\gamma S_j^\alpha + S_i^\alpha S_j^\gamma + S_i^\beta S_j^\gamma + S_i^\gamma S_j^\beta \right) \right], \\ \mathcal{H}_h &= - \sum_i \mathbf{h}_i \cdot \mathbf{S}_i \approx - \sum_i (J_\perp \mathbf{s}_i) \cdot \mathbf{S}_i. \end{aligned} \quad (2)$$

The first part, \mathcal{H}_K , is a Kitaev Hamiltonian with isotropic couplings along the three types of nearest-neighbor (NN) bonds, $\gamma = x, y, z$. The second term, $\mathcal{H}_{J\Gamma\Gamma'}$, includes other symmetry-allowed interactions that are relevant to Kitaev magnets; they consist of first- and third-NN Heisenberg exchanges, J_1 and J_3 , as well as two off-diagonal, bond-dependent couplings, Γ_1 and Γ'_1 . For a given NN γ bond, the latter are defined in terms of a permutation (α, β, γ) of (x, y, z) . Finally, the last part represents the influence of an AFM proximity environment by a Zeeman field \mathbf{h}_i . As advertised, we will assume that this field has a staggered structure

Table 1: Parameter sets utilized in our ED calculations. Both of these models were employed in previous works to reproduce experimental results for α -RuCl₃. The couplings are given in units of meV.

Model	K_1	J_1	Γ_1	Γ'_1	J_3
1 [Ref. 53]	-5.0	-0.5	2.5	0.0	0.5
2 [Ref. 54]	-7.567	-4.750	4.276	2.326	3.400

$\mathbf{h}_i = (-1)^i h \hat{\mathbf{n}}$, with $(-1)^i = \pm 1$ on the A (B) sublattice of the honeycomb lattice.

We expect \mathcal{H}_h to reasonably capture the low-temperature properties of the alluded L_1/L_2 heterostructure if (i) the layers are nearly lattice-matched and (ii) the Néel temperature of L_2 is much higher than that of L_1 . These conditions are met by MnPS₃, which has a Néel temperature $T_N = 78$ K,^{49,50} and together allow one to relate the Zeeman term to an interlayer coupling J_\perp ; see Eq. (2). For concreteness, we fix the direction of the Zeeman field to $\hat{\mathbf{n}} = \frac{1}{\sqrt{3}}(\hat{\mathbf{x}} + \hat{\mathbf{y}} + \hat{\mathbf{z}})$. This coincides with the vector normal to the honeycomb planes in actual Kitaev materials^{5,51} and is consistent with the direction of the easy axis of MnPS₃.⁵²

To restrict the number of free parameters in Eq. (1), we considered two sets of couplings ($K_1, J_1, \Gamma_1, \Gamma'_1, J_3$), which were proposed in Refs. 53 and 54 to describe α -RuCl₃ and are listed in Table 1. As a result, we are left with two free parameters: h and a dimensionless parameter, g , which we will use to interpolate between a pure Kitaev Hamiltonian ($g = 0$) and a more realistic model for α -RuCl₃ ($g = 1$).

We can gain insight into the nature of the ground state at small g and $h/|K_1|$ by performing a perturbative calculation around the Kitaev limit. Specifically, when $g = 0$ and h is much smaller than the two-flux gap $\Delta_{2f} \sim |K_1|$, the Hamiltonian maps onto an effective low-energy model of itinerant Majorana fermions [see the Supporting Information (SI) for details]. As in the case of a uniform magnetic field,⁶ the distinctive feature of this model is that the NN hopping term present at $h = 0$ is supplemented with next-NN hopping processes. However, the staggering of \mathbf{h}_i imprints itself on the sign structure of the hopping amplitudes and thereby *qualitatively* changes the Majorana spectrum at $h \neq 0$. Indeed, instead of becoming gapped, the Dirac cones at the \mathbf{K} and \mathbf{K}' valleys are shifted by opposite energies, so that the system acquires Majorana Fermi surfaces (see Fig. 1) – a result that can also be achieved via a magnetoelectric coupling.⁵⁵

Previous work⁴⁸ revealed a similar mechanism for complex fermions in a variant of the Haldane model.⁵⁶ Much like the systems considered here and in Ref. 55, this model breaks time-reversal symmetry and inversion about the center of a NN bond, but is invariant under the product of those transformations. Remarkably, Ref. 48 also showed that the observed imbalance between the Dirac cones generates *antichiral* edge modes, i.e., copropagating

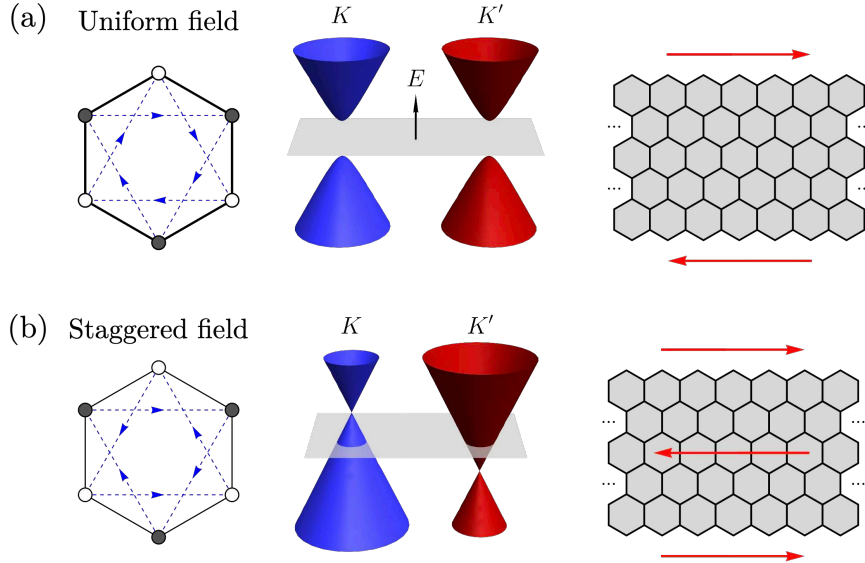


Figure 1: Schematics of the results of third-order perturbation theory in h around the exactly-solvable Kitaev point $g = 0$ for a (a) uniform and (b) staggered external magnetic field. Left: Next-nearest-neighbor Majorana hopping terms induced by the field. The blue arrows are correlated with the sign of the complex hopping amplitudes. Middle: Effect of the perturbations on the Majorana spectrum near the two inequivalent corners, \mathbf{K} and \mathbf{K}' , of the first Brillouin zone. Right: Qualitative difference between the chiral and antichiral edges modes.

currents at the boundary which are compensated by a counterpropagating current in the gapless bulk [see Fig. 1(b)]. Given the similarity to our model, we expect that, regardless of the sign of K_1 , a KSL will develop antichiral edge modes of Majorana fermions when exposed to a weak staggered magnetic field. Therefore, the spin-liquid phase found in this paper at $h \neq 0$ is fundamentally different from the chiral \mathbb{Z}_2 spin liquid^{6,45} obtained under a weak uniform field.

To access phenomena away from the vicinity of the Kitaev point $g = h = 0$, we employed Lanczos ED to the cluster with $N = 24$ sites shown in Fig. 2(a). Among the different 24-site clusters, this particular choice has the advantage of preserving all point-group symmetries of the honeycomb lattice. We imposed periodic boundary conditions and used translational invariance to decompose the Hamiltonian into smaller sectors of well defined momentum \mathbf{k} . Ground-state phase diagrams were then constructed by performing scans at constant g or h . We determined phase boundaries by identifying the ground-state sector \mathbf{k} and monitoring mainly two types of quantities: the second derivatives of the ground-state energy, $\partial^2 E_{\text{gs}}/\partial g^2$ and $\partial^2 E_{\text{gs}}/\partial h^2$, and the fidelity $\mathcal{F}(\mathbf{x}) = |\langle \psi(\mathbf{x} + \delta\mathbf{x}) | \psi(\mathbf{x}) \rangle|$, which measures the overlap between ground-state wavefunctions at neighboring points $\mathbf{x} = (g, h)$ and $\mathbf{x} + \delta\mathbf{x}$ with $\delta\mathbf{x} = (\delta g, 0)$ or $(0, \delta h)$. Finally, to characterize the different phases obtained in our

simulations, we computed the static spin structure factor

$$\mathcal{S}(\mathbf{q}) = \frac{1}{N} \sum_{i,j} e^{i\mathbf{q}\cdot(\mathbf{r}_i-\mathbf{r}_j)} \langle \mathbf{S}_i \cdot \mathbf{S}_j \rangle \quad (3)$$

and two-point correlation functions

$$C^{\alpha\beta}(r) = \langle S_0^\alpha S_r^\beta \rangle \quad (4)$$

with respect to a fixed reference site 0. In both cases, $\langle \dots \rangle$ denotes the ground-state expectation value.

The ED results for the phase diagrams of Models 1 and 2 are shown in Figs. 2(c) and 2(d), respectively. At $g = 0$, both models are identical up to a rescaling of $|K_1|$ and undergo a sequence of three phase transitions. Starting at low fields, the antichiral KSL gives way to a narrow intermediate phase which extends from $h_{c1} \approx 0.4625|K_1|$ to $h_{c2} \approx 0.4775|K_1|$. In this process, the ground-state sector briefly changes from $\mathbf{k} = \mathbf{\Gamma}$ to \mathbf{K} before returning to $\mathbf{k} = \mathbf{\Gamma}$ in a second intermediate phase that remains stable up to $h_{c3} \approx 0.575|K_1|$. Above this threshold, the system enters a (partially) polarized state with neither symmetry-breaking nor topological order. These results are mostly consistent with previous simulations by Hickey and Trebst;⁴⁵ the only disagreement lies in the existence of the phase between h_{c1} and h_{c2} , which may have been overlooked until now due to its small extent and different momentum sector.

In contrast, when $h = 0$, both models exhibit a single phase transition between the KSL and the zigzag phase as g is tuned from 0 to 1. The transition occurs at $g_c \approx 0.17$ for Model 1 and at a lower $g_c \approx 0.11$ for Model 2 due to stronger non-Kitaev couplings. Although one can already infer that the second phase corresponds to zigzag magnetic order by adiabatic continuity to $g = 1$, we confirmed that this is the case by analyzing the static structure factor, Eq. (3), and two-point correlations, Eq. (4), of the ground-state wavefunction.

A comparison between Figs. 2(c,d) for $g, h \neq 0$ reveals that Model 1 has a richer phase diagram, with a higher number of field-induced phases at small g . In particular, there are two phases, colored light blue and purple in Fig. 2(c), which occur only for $g \neq 0$. Most interesting among the two is the purple phase, which displays short-range spin-spin correlations, but differs from the KSL in two main aspects. The first is that it belongs to the momentum sector $\mathbf{k} = \mathbf{K}$, and therefore behaves nontrivially under translations. The second and most significant difference is illustrated in Fig. 2(e), which compares results for the diagonal components $C^{\alpha\alpha}$ ($\alpha = x, y, z$) of the spin-spin correlation functions in the KSL and in the purple phase (right panel). While both phases maximize each $|C^{\alpha\alpha}|$ along the

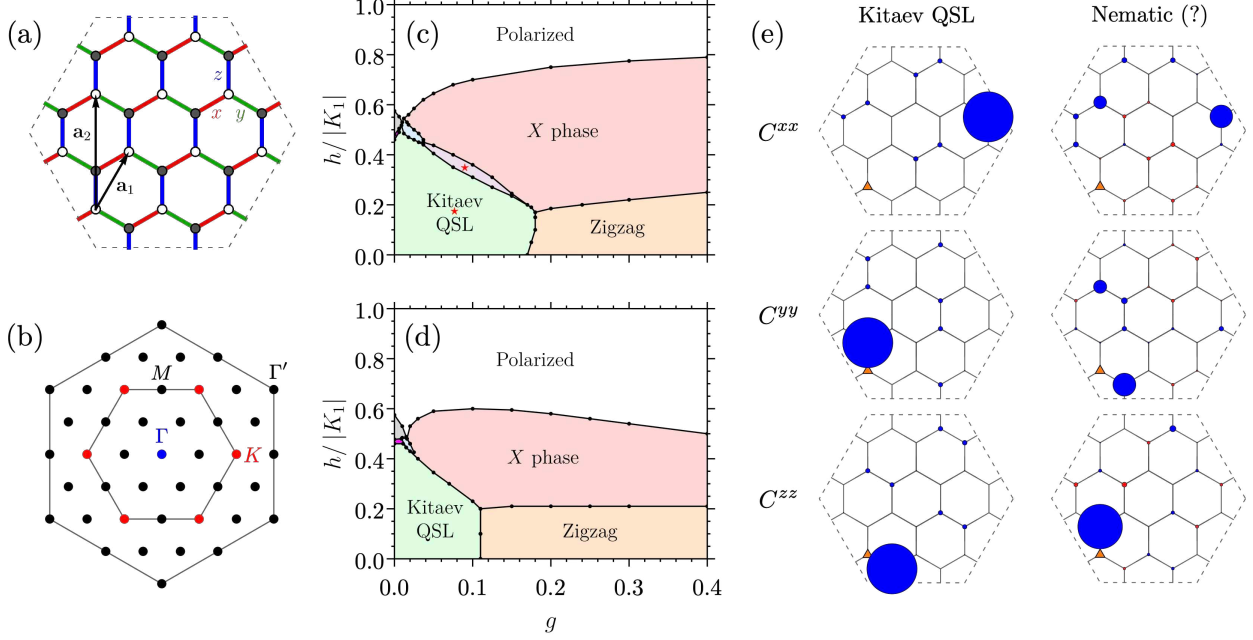


Figure 2: (a) 24-site cluster used for our ED calculations. (b) Momentum resolution of the finite-size cluster. The inner hexagon represents the first Brillouin zone, whereas the outer hexagon connects the six equivalent Γ' points. (c,d) Ground-state phase diagrams of Models 1 and 2 from Table 1. Both models exhibit a robust field-induced X phase which precedes polarization for nearly all values of g up to 1. (e) Comparison between two-point correlations $C^{\alpha\alpha}$ relative to site 0 (orange triangle) in the KSL and the purple phase above it in (c). The data were obtained for $(g, h/|K_1|) = (0.075, 0.175)$ and $(0.09, 0.35)$, which are highlighted in (c). The value of $C^{\alpha\alpha}$ at each site is represented by a circle whose radius is proportional to $|C^{\alpha\alpha}|$ and whose color reflects the sign of $C^{\alpha\alpha}$. Blue (red) circles indicate FM (AFM) correlations.

corresponding NN α -bond,⁵⁷ the purple phase develops stronger correlations along one of the three possible directions (z bonds in the present example). Hence, in contrast to the KSL, it breaks the C_3^* symmetry of the Hamiltonian,⁵¹ which combines $2\pi/3$ rotations of the honeycomb lattice with a simultaneous $2\pi/3$ rotation of the spin operators around the out-of-plane axis $\hat{\mathbf{n}}$. Together with a broad but anisotropic spin structure factor, this suggests that the purple phase realizes a type of nematic order.

Despite the above differences, the phase diagrams of Models 1 and 2 are mostly occupied by the same *four* phases. Besides the expected Kitaev, zigzag, and field-polarized phases, we encounter a robust phase at intermediate fields, which is shown in pink in Figs. 2(c,d) and will henceforth be referred to as the “ X phase”. This phase spans a broad interval $0.02 \lesssim g \leq 1$ and, upon increasing h , generally reaches a field-polarized state via a first-order transition. Its spin structure factor, depicted in Fig. 3(a) for a representative point $(g, h/|K_1|) = (0.17, 0.50)$, exhibits primary and secondary peaks at the Γ' and $\mathbf{K}/2$ points,

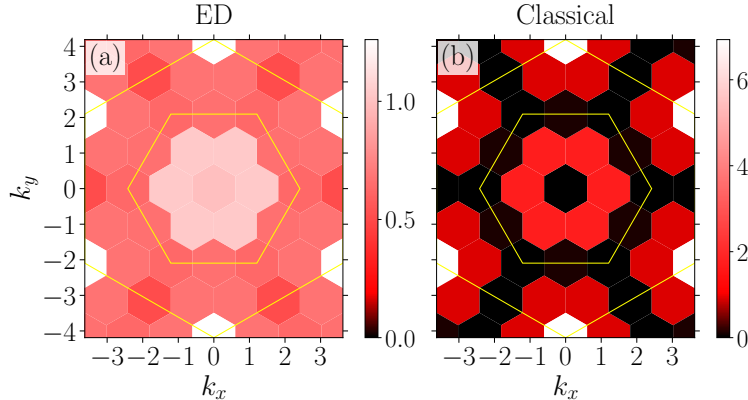


Figure 3: Static spin structure factor $\mathcal{S}(\mathbf{k})$ obtained by applying (a) ED and (b) a classical energy-minimization method to Model 1 on the 24-site cluster shown in Fig. 2(a). The results were obtained for the points $(g, h/|K_1|) = (0.17, 0.50)$ and $(0.75, 1.18)$, respectively. The yellow hexagons have the same meaning as in Fig. 2(b).

respectively. While the former reflect the development of a staggered magnetization induced by h , the latter suggest that the X phase displays long-range magnetic order. However, with our implementation of ED, we are unable to discern whether this is a single- \mathbf{Q} spin spiral or, potentially, a more exotic triple- \mathbf{Q} state.

To address this issue, we sought a classical analog of the X phase on the same 24-site cluster employed in our ED calculations. Using an iterative energy-minimization method (see SI for details), we searched for ground states of the classical version of Model 1, in which spins \mathbf{S}_i are treated as unit vectors, over a wide range of g and h . Among the various phases we encountered, none were single- \mathbf{Q} spirals with an ordering wavevector $\mathbf{Q} = \mathbf{K}/2$. However, we did obtain a triple- \mathbf{Q} ground state whose structure factor, depicted in Fig. 3(b) for $(g, h/|K_1|) = (0.75, 1.18)$, shows the same distinctive features as Fig. 3(a): primary peaks at Γ' accompanied by local maxima at $\mathbf{K}/2$. Although the absence of quantum fluctuations causes Fig. 3(b) to have notably sharper features than Fig. 3(a), the overall resemblance between the two cases indicates that the X phase identified within 24-site ED corresponds to a triple- \mathbf{Q} magnetically ordered state.

As a next step, we aimed to determine whether the above triple- \mathbf{Q} configuration is still a classical ground state of Model 1 for larger system sizes. To this end, we applied the same classical method as before to 21 clusters of varying shapes and sizes (see SI). We imposed periodic boundary conditions in all cases and reached a maximum of $N = 288$ sites. Working at a fixed $g = 0.75$, we then selected the states with the lowest energy per spin for values of $h/|K_1| \in [0, 2]$. Our results, compiled in Fig. 4, show that the system undergoes a complex magnetization process before entering the field-polarized phase. As in the case

of a spatially uniform field, this follows not only from the presence of magnetic frustration, but also from the nontrivial interplay between the magnetic field and the anisotropic spin interactions.^{51,58–61}

Upon increasing h , the low-field zigzag (ZZ) phase is suppressed at $h/|K_1| \approx 0.19$, giving way to a sequence of three types of skyrmion crystals (SkXs), i.e., triple- \mathbf{Q} states whose spin textures display a periodic arrangement of topological defects. These defects are characterized by the presence of nontrivial topological charges n_{sk}^μ on the triangular sublattices $\mu = A, B$ of the honeycomb lattice (see SI).

The first SkX occurs within the extended interval $0.19 < h/|K_1| < 1.09$ and has opposite topological charges on each sublattice, $(n_{\text{sk}}^A, n_{\text{sk}}^B) = (-1, +1)$. Its structure factor exhibits pronounced Bragg peaks at the three inequivalent \mathbf{M} points (see Fig. 4(b), left). By inspecting the spin configuration directly in real space, we find that it has an 8-site magnetic unit cell and corresponds to a state dubbed AFM star in an early study of the classical Heisenberg-Kitaev model in a *uniform* magnetic field.⁵⁸ Later on, this same type of order was suggested as a potential ground state of the Kitaev material $\text{Na}_2\text{Co}_2\text{TeO}_6$ in zero field.^{62–66} Here, it is intriguing that the AFM star phase is absent from the quantum phase diagrams of Figs. 2(c,d), since it occupies a broad region in Fig. 4 and is commensurate with the 24-site cluster in Fig. 2(a). This may be due to the fragility of the state to quantum fluctuations, which was demonstrated within the framework of a $1/S$ expansion in Ref. 67.

The second and third SkXs, henceforth labeled SkX_2 and SkX_3 , are built from a linear combination of ordering wavevectors $\mathbf{Q} = 3\mathbf{K}/7 \approx 0.43\mathbf{K}$ and $\mathbf{Q} = 0.4\mathbf{K}$, respectively. Thus, they have larger magnetic unit cells than an AFM star state [see Figs. 4(c,d)] and, given the greater proximity to $\mathbf{Q} = \mathbf{K}/2$, are better candidates for a classical analog of the X phase. Similarly to the AFM star, SkX_2 is an AFM SkX with topological charges $(n_{\text{sk}}^A, n_{\text{sk}}^B) = (-1, +1)$. SkX_3 , on the other hand, is characterized by two different, yet equally favorable, set of integers: $(n_{\text{sk}}^A, n_{\text{sk}}^B) = (-3, +1)$ and $(-1, +3)$. This indicates that SkX_3 *spontaneously* develops a net topological charge of ± 2 per magnetic unit cell, a behavior reminiscent of the “ferrichiral” skyrmion phase identified in a recent study of an extended Kitaev model on the triangular lattice.⁶⁸

Finally, the system realizes a sequence of topologically trivial ($n_{\text{sk}}^\mu = 0$) triple- \mathbf{Q} phases between $h/|K_1| = 1.37$ and 1.62 before reaching the field-polarized phase. While we refrain from describing these triple- \mathbf{Q} states in detail, it is worth noting that the norm Q of their ordering wavevectors consistently decreases with increasing h . This extends a trend already seen among the three aforementioned SkXs and hints at the possible existence of an even greater number of triple- \mathbf{Q} phases, both topological and trivial, in the thermodynamic limit. It also implies that, among all classical phases obtained here, the one whose

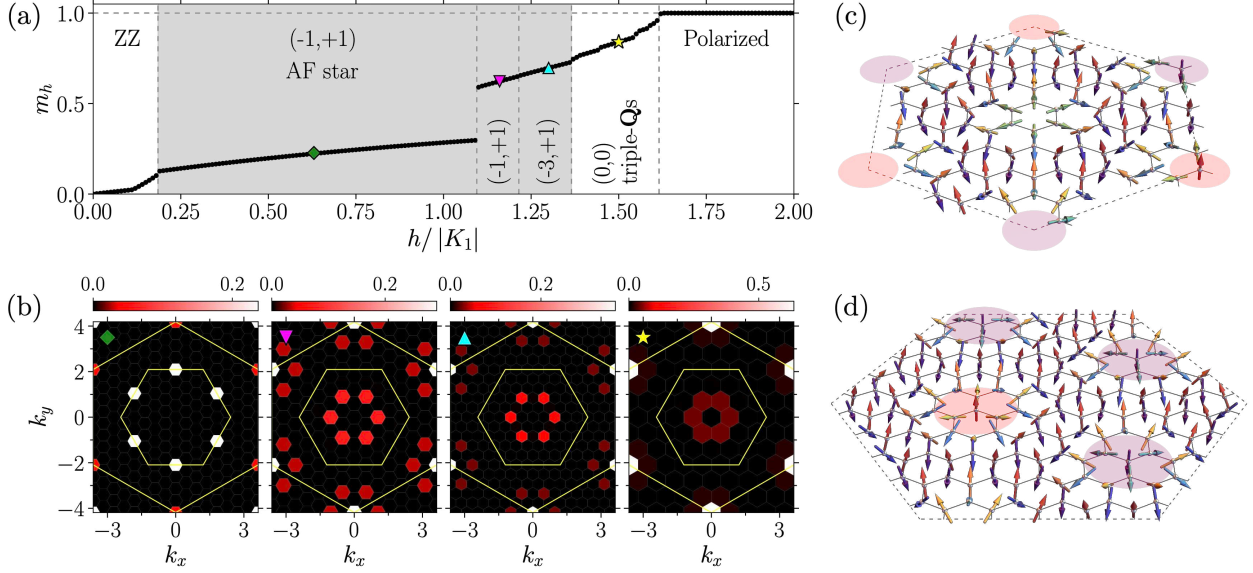


Figure 4: Results obtained from classical energy minimization for Model 1 at fixed $g = 0.75$. (a) Staggered magnetization per site, $m_h = -(Nh)^{-1} \sum_i \mathbf{h}_i \cdot \mathbf{S}_i$, as a function of h . Between the zigzag (ZZ) and polarized phases, the system realizes a sequence of SkXs (gray shaded region) and topologically trivial triple- \mathbf{Q} phases with progressively smaller ordering wavevectors. The former are characterized by their sublattice-resolved topological charges, $(n_{\text{sk}}^A, n_{\text{sk}}^B)$. (b) Static structure factors per site, $\mathcal{S}(\mathbf{k})/N$, for the four points highlighted in the magnetization curve. Data are shown for the discrete momenta compatible with the clusters on which the solutions were obtained. The inner yellow hexagon delineates the first Brillouin zone. (c,d) Magnetic unit cells of the $(-1, +1)$ and $(-3, +1)$ SkXs, respectively. Shaded disks highlight the location of skyrmions.

ordering wavevectors are closest to $\mathbf{K}/2$ is SkX₂. Given the limited momentum resolution of our 24-site ED, this does not unambiguously identify the X phase as SkX₂. However, it signals that applying staggered magnetic fields to Kitaev materials may be a promising route to realize SkXs with a net topological charge and periodicities that are smaller than their metallic counterparts stabilized by the Dzyaloshinskii–Moriya interaction.⁶⁹

Given that the SkX₂ and SkX₃ states would have a periodicity of ~ 20 nm in α -RuCl₃, they may be detectable via Lorentz transmission electron microscopy⁷⁰ or magnetic exchange force microscopy.^{71,72} Both of these methods are well-suited to image magnetic configurations in thin insulating films and have high spatial resolutions of ~ 10 nm and $\lesssim 1$ nm, respectively. SkX₂ and SkX₃ may also display topological magnon bands and an associated (non-quantized) thermal Hall effect.^{73–75}

As mentioned above, a plausible materials platform to scrutinize a Kitaev material subject to a *staggered* magnetic field is a bilayer of α -RuCl₃ and AFM MnPS₃. To obtain a characteristic coupling scale for this heterostructure, we use density functional theory cal-

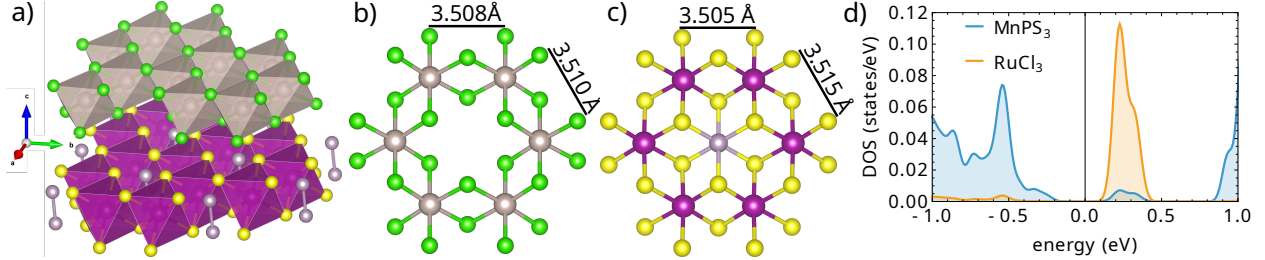


Figure 5: (a) Structure of the bilayer α -RuCl₃/MnPS₃. Ru:gray, Cl:green, Mn:purple, S:yellow, P:silver (b,c) Single layers of α -RuCl₃ and MnPS₃, respectively, showing cation-cation distances. (d) Density of states for a fully ferromagnetic configuration (interlayer anti-ferromagnetic configuration is qualitatively similar).

culations. We start by building the structure of a heterobilayer as shown in Fig. 5(a) that is subsequently optimized. Further details about the methodology, including relaxation of the structure, are provided in the SI. Figures 5(b,c) show relevant bond lengths for MnPS₃ and α -RuCl₃ in our relaxed structure, reflecting that they are nearly lattice-matched. We subsequently use the optimized structure to calculate the energy difference between two magnetic states both with FM order within the layers and differing by the alignment or anti-alignment between the layers. Importantly, there is no charge transfer between the layers and the system remains in an insulating state regardless of the interlayer orientation, as shown in Fig. 5(c). We obtain an effective interlayer exchange $h \simeq 0.3$ meV, which alone is not enough to enable access to the X phase. It may be possible to apply out-of-plane pressure to decrease the interlayer spacing and increase the coupling.

In summary, we studied two-dimensional extended Kitaev models subject to an effective staggered magnetic field. We showed that, in addition to inducing Majorana Fermi surfaces and *antichiral* edge modes in the KSL, the staggered field can give rise to a nonmagnetic nematic phase and to SkXs, both with and without a net topological charge. We then complemented these results by employing first-principle simulations to assess the prospect of realizing these phenomena in an α -RuCl₃/MnPS₃ bilayer. Our DFT calculations demonstrate that this heterostructure is approximately lattice-matched and MnPS₃ leads to an effective field of about $h \simeq 0.3$ meV.

An interesting direction for future research would be to consider how a Kitaev material is influenced by a proximity-induced magnetic field \mathbf{h}_i with the periodicity of a moiré superlattice. This would account for the small lattice mismatch between MnPS₃ and α -RuCl₃ layers and might lead to further interesting phenomena. On the materials front, it would be worthwhile not only to pursue an experimental realization of the α -RuCl₃/MnPS₃ heterobilayer, but also to seek other material platforms capable of reproducing the physics discussed here.

Associated Content

Supporting Information

Contains further details on the perturbative calculation around the Kitaev limit, exact diagonalization, iterative energy-minimization algorithm, and computation of the topological charges and details on the density-functional theory calculations. Includes Refs.⁷⁶⁻⁸⁰

Author Information

Corresponding Author: Onur Erten - onur.erten@asu.edu & Antia Botana - asanc157@asu.edu

Author Contributions: PMC, JK, ASB, and OE conceived and designed the project. PMC performed the perturbative analysis, exact-diagonalization calculations, and classical simulations. EDR and ASB carried out the first-principles calculations. All authors analyzed the results and contributed to writing the manuscript.

Notes: The authors declare no competing financial interest.

Acknowledgements

We thank Hui-Ke Jin for preliminary DMRG calculations, as well as Eric C. Andrade and Natalia Perkins for helpful discussions. P.M.C. is also grateful to Eric C. Andrade, Niccolò Francini, Lukas Janssen, and Matthias Vojta for collaborations on related projects. This work is supported by the U.S. Department of Energy, Office of Science, Office of Basic Energy Sciences, Material Sciences and Engineering Division under Award Number DE-SC0025247. EDR and ASB acknowledge the support of NSF Grant No. DMR-2206987. J. K. acknowledges support from the Deutsche Forschungsgemeinschaft (DFG, German Research Foundation) grant TRR 360 - 492547816 [14]. J.K. further acknowledges support from DFG under Germany's Excellence Strategy (EXC-2111-390814868), DFG Grants No. KN1254/1-2, KN1254/2-1 and SFB 1143 (project-id 247310070), as well as the Munich Quantum Valley, which is supported by the Bavarian state government with funds from the Hightech Agenda Bayern Plus. J.K. further acknowledges support from the Imperial-TUM flagship partnership, as well as the Keck Foundation. The authors acknowledge Research Computing at Arizona State University for providing HPC resources⁸¹ that contributed to the results reported in this paper.

References

- (1) Savary, L.; Balents, L. Quantum spin liquids: a review. *Rep. Prog. Phys.* **2016**, *80*, 016502.
- (2) Zhou, Y.; Kanoda, K.; Ng, T.-K. Quantum spin liquid states. *Rev. Mod. Phys.* **2017**, *89*, 025003.
- (3) Knolle, J.; Moessner, R. A Field Guide to Spin Liquids. *Annu. Rev. Condens. Matter Phys.* **2019**, *10*, 451.
- (4) Broholm, C.; Cava, R. J.; Kivelson, S. A.; Nocera, D. G.; Norman, M. R.; Senthil, T. Quantum spin liquids. *Science* **2020**, *367*, 263.
- (5) Trebst, S.; Hickey, C. Kitaev materials. *Phys. Rep.* **2022**, *950*, 1–37.
- (6) Kitaev, A. Anyons in an exactly solved model and beyond. *Ann. Phys.* **2006**, *321*, 2–111.
- (7) Jackeli, G.; Khaliullin, G. Mott Insulators in the Strong Spin-Orbit Coupling Limit: From Heisenberg to a Quantum Compass and Kitaev Models. *Phys. Rev. Lett.* **2009**, *102*, 017205.
- (8) Chaloupka, J.; Jackeli, G.; Khaliullin, G. Kitaev-Heisenberg Model on a Honeycomb Lattice: Possible Exotic Phases in Iridium Oxides $A_2\text{IrO}_3$. *Phys. Rev. Lett.* **2010**, *105*, 027204.
- (9) Chaloupka, J.; Jackeli, G.; Khaliullin, G. Zigzag Magnetic Order in the Iridium Oxide Na_2IrO_3 . *Phys. Rev. Lett.* **2013**, *110*, 097204.
- (10) Rau, J. G.; Lee, E. K.-H.; Kee, H.-Y. Generic Spin Model for the Honeycomb Iridates beyond the Kitaev Limit. *Phys. Rev. Lett.* **2014**, *112*, 077204.
- (11) Winter, S. M.; Li, Y.; Jeschke, H. O.; Valentí, R. Challenges in design of Kitaev materials: Magnetic interactions from competing energy scales. *Phys. Rev. B* **2016**, *93*, 214431.
- (12) Winter, S. M.; Tsirlin, A. A.; Daghofer, M.; van den Brink, J.; Singh, Y.; Gegenwart, P.; Valentí, R. Models and materials for generalized Kitaev magnetism. *J. Phys.: Condens. Matter* **2017**, *29*, 493002.

- (13) Rousochatzakis, I.; Perkins, N. B.; Luo, Q.; Kee, H.-Y. Beyond Kitaev physics in strong spin-orbit coupled magnets. **2023**, arXiv:2308.01943. *arXiv.org e-Print archive.*, <https://arxiv.org/abs/2308.01943> (accessed on August 03, 2023).
- (14) Plumb, K. W.; Clancy, J. P.; Sandilands, L. J.; Shankar, V. V.; Hu, Y. F.; Burch, K. S.; Kee, H.-Y.; Kim, Y.-J. α -RuCl₃: A spin-orbit assisted Mott insulator on a honeycomb lattice. *Phys. Rev. B* **2014**, *90*, 041112.
- (15) Johnson, R. D.; Williams, S.; Haghighirad, A.; Singleton, J.; Zapf, V.; Manuel, P.; Mazin, I.; Li, Y.; Jeschke, H. O.; Valentí, R.; Coldea, R. Monoclinic crystal structure of α -RuCl₃ and the zigzag antiferromagnetic ground state. *Phys. Rev. B* **2015**, *92*, 235119.
- (16) Sears, J. A.; Songvilay, M.; Plumb, K. W.; Clancy, J. P.; Qiu, Y.; Zhao, Y.; Parshall, D.; Kim, Y.-J. Magnetic order in α – RuCl₃: A honeycomb-lattice quantum magnet with strong spin-orbit coupling. *Phys. Rev. B* **2015**, *91*, 144420.
- (17) Cao, H. B.; Banerjee, A.; Yan, J.-Q.; Bridges, C. A.; Lumsden, M. D.; Mandrus, D. G.; Tennant, D. A.; Chakoumakos, B. C.; Nagler, S. E. Low-temperature crystal and magnetic structure of α -RuCl₃. *Phys. Rev. B* **2016**, *93*, 134423.
- (18) Banerjee, A. et al. Proximate Kitaev quantum spin liquid behaviour in a honeycomb magnet. *Nat. Mater.* **2016**, *15*, 733–740.
- (19) Banerjee, A.; Yan, J.; Knolle, J.; Bridges, C. A.; Stone, M. B.; Lumsden, M. D.; Mandrus, D. G.; Tennant, D. A.; Moessner, R.; Nagler, S. E. Neutron scattering in the proximate quantum spin liquid α -RuCl₃. *Science* **2017**, *356*, 1055–1059.
- (20) Ojeda-Aristizabal, C. et al. Lessons from α -RuCl₃ for pursuing quantum spin liquid physics in atomically thin materials. 2025; <https://arxiv.org/abs/2511.13838>.
- (21) Sears, J. A.; Zhao, Y.; Xu, Z.; Lynn, J. W.; Kim, Y.-J. Phase diagram of α – RuCl₃ in an in-plane magnetic field. *Phys. Rev. B* **2017**, *95*, 180411.
- (22) Wolter, A. U. B.; Corredor, L. T.; Janssen, L.; Nenkov, K.; Schönecker, S.; Do, S.-H.; Choi, K.-Y.; Albrecht, R.; Hunger, J.; Doert, T.; Vojta, M.; Büchner, B. Field-induced quantum criticality in the Kitaev system α – RuCl₃. *Phys. Rev. B* **2017**, *96*, 041405.
- (23) Kasahara, Y.; Ohnishi, T.; Mizukami, Y.; Tanaka, O.; Ma, S.; Sugii, K.; Kurita, N.; Tanaka, H.; Nasu, J.; Motome, Y.; Shibauchi, T.; Matsuda, Y. Majorana quantization

- and half-integer thermal quantum Hall effect in a Kitaev spin liquid. *Nature* **2018**, *559*, 227–231.
- (24) Yokoi, T.; Ma, S.; Kasahara, Y.; Kasahara, S.; Shibauchi, T.; Kurita, N.; Tanaka, H.; Nasu, J.; Motome, Y.; Hickey, C.; Trebst, S.; Matsuda, Y. Half-integer quantized anomalous thermal Hall effect in the Kitaev material candidate α -RuCl₃. *Science* **2021**, *373*, 568–572.
- (25) Gass, S.; C onsoli, P. M.; Kocsis, V.; Corredor, L. T.; Lampen-Kelley, P.; Mandrus, D. G.; Nagler, S. E.; Janssen, L.; Vojta, M.; B uchner, B.; Wolter, A. U. B. Field-induced transitions in the Kitaev material α -RuCl₃ probed by thermal expansion and magnetostriction. *Phys. Rev. B* **2020**, *101*, 245158.
- (26) Lefran ois,  ..; Grissonnanche, G.; Baglo, J.; Lampen-Kelley, P.; Yan, J.-Q.; Balz, C.; Mandrus, D.; Nagler, S.; Kim, S.; Kim, Y.-J.; others Evidence of a Phonon Hall Effect in the Kitaev Spin Liquid Candidate α -RuCl₃. *Phys. Rev. X* **2022**, *12*, 021025.
- (27) Bruin, J. A. N.; Claus, R. R.; Matsumoto, Y.; Kurita, N.; Tanaka, H.; Takagi, H. Robustness of the thermal Hall effect close to half-quantization in α -RuCl₃. *Nat. Phys.* **2022**, *18*, 401–405.
- (28) Czajka, P.; Gao, T.; Hirschberger, M.; Lampen-Kelley, P.; Banerjee, A.; Quirk, N.; Mandrus, D. G.; Nagler, S. E.; Ong, N. P. Planar thermal Hall effect of topological bosons in the Kitaev magnet α -RuCl₃. *Nat. Mater.* **2023**, *22*, 36–41.
- (29) Sarkis, C. L.; Dixit, K. D.; Rao, P.; Khundzakishvili, G.; Balz, C.; Yan, J.-Q.; Winn, B.; Williams, T. J.; Unnikrishnan, A.; Moessner, R.; Tennant, D. A.; Knolle, J.; Nagler, S. E.; Banerjee, A. Intermediate Field Spin(on) Dynamics in α -RuCl₃. 2026; <https://arxiv.org/abs/2601.16850>.
- (30) Bastien, G.; Roslova, M.; Haghighi, M.; Mehlawat, K.; Hunger, J.; Isaeva, A.; Doert, T.; Vojta, M.; B uchner, B.; Wolter, A. Spin-glass state and reversed magnetic anisotropy induced by Cr doping in the Kitaev magnet α -RuCl₃. *Phys. Rev. B* **2019**, *99*, 214410.
- (31) Bastien, G.; Garbarino, G.; Yadav, R.; Mart inez-Casado, F. J.; Rodr iguez, R. B.; Stahl, Q.; Kusch, M.; Limandri, S. P.; Ray, R.; Lampen-Kelley, P.; others Pressure-induced dimerization and valence bond crystal formation in the Kitaev-Heisenberg magnet α -RuCl₃. *Phys. Rev. B* **2018**, *97*, 241108.

- (32) Bachus, S.; Kaib, D. A.; Tokiwa, Y.; Jesche, A.; Tsurkan, V.; Loidl, A.; Winter, S. M.; Tsirlin, A. A.; Valenti, R.; Gegenwart, P. Thermodynamic Perspective on Field-Induced Behavior of α -RuCl₃. *Phys. Rev. Lett.* **2020**, *125*, 097203.
- (33) Kaib, D. A.; Biswas, S.; Riedl, K.; Winter, S. M.; Valentí, R. Magnetoelastic coupling and effects of uniaxial strain in α -RuCl₃ from first principles. *Phys. Rev. B* **2021**, *103*, L140402.
- (34) Kocsis, V.; Kaib, D. A.; Riedl, K.; Gass, S.; Lampen-Kelley, P.; Mandrus, D. G.; Nagler, S. E.; Pérez, N.; Nielsch, K.; Büchner, B.; others Magnetoelastic coupling anisotropy in the Kitaev material α -RuCl₃. *Phys. Rev. B* **2022**, *105*, 094410.
- (35) Akram, M.; Kapeghian, J.; Das, J.; Valentí, R.; Botana, A. S.; Erten, O. Theory of Moiré Magnetism in Twisted Bilayer α -RuCl₃. *Nano Letters* **2024**, *24*, 890–896.
- (36) Mashhadi, S.; Kim, Y.; Kim, J.; Weber, D.; Taniguchi, T.; Watanabe, K.; Park, N.; Lotsch, B.; Smet, J. H.; Burghard, M.; others Spin-split band hybridization in graphene proximitized with α -RuCl₃ nanosheets. *Nano Letters* **2019**, *19*, 4659–4665.
- (37) Zhou, B.; Balgley, J.; Lampen-Kelley, P.; Yan, J.-Q.; Mandrus, D. G.; Henriksen, E. A. Evidence for charge transfer and proximate magnetism in graphene- α -RuCl₃ heterostructures. *Phys. Rev. B* **2019**, *100*, 165426.
- (38) Biswas, S.; Li, Y.; Winter, S. M.; Knolle, J.; Valentí, R. Electronic Properties of α -RuCl₃ in proximity to graphene. *Phys. Rev. Lett.* **2019**, *123*, 237201.
- (39) Rizzo, D. J. et al. Charge-Transfer Plasmon Polaritons at Graphene/ α -RuCl₃ Interfaces. *Nano Letters* **2020**, *20*, 8438–8445.
- (40) Gerber, E.; Yao, Y.; Arias, T. A.; Kim, E.-A. Ab Initio Mismatched Interface Theory of Graphene on α -RuCl₃: Doping and Magnetism. *Phys. Rev. Lett.* **2020**, *124*, 106804.
- (41) Leeb, V.; Polyudov, K.; Mashhadi, S.; Biswas, S.; Valentí, R.; Burghard, M.; Knolle, J. Anomalous quantum oscillations in a heterostructure of graphene on a proximate quantum spin liquid. *Phys. Rev. Lett.* **2021**, *126*, 097201.
- (42) Balgley, J.; Butler, J.; Biswas, S.; Ge, Z.; Lagasse, S.; Taniguchi, T.; Watanabe, K.; Cothrine, M.; Mandrus, D. G.; Velasco Jr, J.; others Ultrasharp Lateral p-n Junctions in Modulation-Doped Graphene. *Nano Letters* **2022**, *22*, 4124–4130.

- (43) Shi, J.; MacDonald, A. Magnetic states of graphene proximitized Kitaev materials. *Phys. Rev. B* **2023**, *108*, 064401.
- (44) Zhang, L.; Motome, Y. Possible Realization of Kitaev Spin Liquids in van Der Waals Heterostructures of RuCl_3 and CrX_3 ($X=\text{Cl}$ and I). *Phys. Rev. B* **2024**, *110*, L241109.
- (45) Hickey, C.; Trebst, S. Emergence of a field-driven $U(1)$ spin liquid in the Kitaev honeycomb model. *Nat. Commun.* **2019**, *10*, 530.
- (46) Liu, H.; Khaliullin, G. Pseudospin exchange interactions in d^7 cobalt compounds: Possible realization of the Kitaev model. *Phys. Rev. B* **2018**, *97*, 014407.
- (47) Sano, R.; Kato, Y.; Motome, Y. Kitaev-Heisenberg Hamiltonian for high-spin d^7 Mott insulators. *Phys. Rev. B* **2018**, *97*, 014408.
- (48) Colomés, E.; Franz, M. Antichiral Edge States in a Modified Haldane Nanoribbon. *Phys. Rev. Lett.* **2018**, *120*, 086603.
- (49) Kurosawa, K.; Saito, S.; Yamaguchi, Y. Neutron Diffraction Study on MnPS_3 and FePS_3 . *J. Phys. Soc. Jpn.* **1983**, *52*, 3919–3926.
- (50) Wildes, A. R.; Roessli, B.; Lebech, B.; Godfrey, K. W. Spin waves and the critical behaviour of the magnetization in MnPS_3 . *J. Phys.: Condens. Matter* **1998**, *10*, 6417.
- (51) Janssen, L.; Vojta, M. Heisenberg–Kitaev physics in magnetic fields. *J. Phys.: Condens. Matter* **2019**, *31*, 423002.
- (52) Han, H.; Lin, H.; Gan, W.; Xiao, R.; Liu, Y.; Ye, J.; Chen, L.; Wang, W.; Zhang, L.; Zhang, C.; Li, H. Field-induced spin reorientation in the Néel-type antiferromagnet MnPS_3 . *Phys. Rev. B* **2023**, *107*, 075423.
- (53) Winter, S. M.; Riedl, K.; Maksimov, P. A.; Chernyshev, A. L.; Honecker, A.; Valentí, R. Breakdown of magnons in a strongly spin-orbital coupled magnet. *Nat. Commun.* **2017**, *8*, 1152.
- (54) Möller, M.; Maksimov, P. A.; Jiang, S.; White, S. R.; Valentí, R.; Chernyshev, A. L. Rethinking $\alpha\text{-RuCl}_3$: Parameters, models, and phase diagram. *Phys. Rev. B* **2025**, *112*, 104403.
- (55) Chari, R.; Moessner, R.; Rau, J. G. Magnetoelectric generation of a Majorana-Fermi surface in Kitaev’s honeycomb model. *Phys. Rev. B* **2021**, *103*, 134444.

- (56) Haldane, F. D. M. Model for a Quantum Hall Effect without Landau Levels: Condensed-Matter Realization of the “Parity Anomaly”. *Phys. Rev. Lett.* **1988**, *61*, 2015–2018.
- (57) Baskaran, G.; Mandal, S.; Shankar, R. Exact Results for Spin Dynamics and Fractionalization in the Kitaev Model. *Phys. Rev. Lett.* **2007**, *98*, 247201.
- (58) Janssen, L.; Andrade, E. C.; Vojta, M. Honeycomb-Lattice Heisenberg-Kitaev Model in a Magnetic Field: Spin Canting, Metamagnetism, and Vortex Crystals. *Phys. Rev. Lett.* **2016**, *117*, 277202.
- (59) Janssen, L.; Andrade, E. C.; Vojta, M. Magnetization processes of zigzag states on the honeycomb lattice: Identifying spin models for α -RuCl₃ and Na₂IrO₃. *Phys. Rev. B* **2017**, *96*, 064430.
- (60) Chern, G.-W.; Sizyuk, Y.; Price, C.; Perkins, N. B. Kitaev-Heisenberg model in a magnetic field: Order-by-disorder and commensurate-incommensurate transitions. *Phys. Rev. B* **2017**, *95*, 144427.
- (61) Chern, L. E.; Kaneko, R.; Lee, H.-Y.; Kim, Y. B. Magnetic field induced competing phases in spin-orbital entangled Kitaev magnets. *Phys. Rev. Res.* **2020**, *2*, 013014.
- (62) Chen, W.; Li, X.; Hu, Z.; Hu, Z.; Yue, L.; Sutarto, R.; He, F.; Iida, K.; Kamazawa, K.; Yu, W.; Lin, X.; Li, Y. Spin-orbit phase behavior of Na₂Co₂TeO₆ at low temperatures. *Phys. Rev. B* **2021**, *103*, L180404.
- (63) Krüger, W. G. F.; Chen, W.; Jin, X.; Li, Y.; Janssen, L. Triple-q Order in Na₂Co₂TeO₆ from Proximity to Hidden-SU(2)-Symmetric Point. *Phys. Rev. Lett.* **2023**, *131*, 146702.
- (64) Gu, Y.; Jin, X.; Li, Y. On the Multi-q Characteristics of Magnetic Ground States of Honeycomb Cobalt Oxides. *Chin. Phys. Lett.* **2025**, *42*, 027303.
- (65) Francini, N.; Janssen, L. Ferrimagnetism from triple-q order in Na₂Co₂TeO₆. *Phys. Rev. B* **2024**, *110*, 235118.
- (66) Francini, N.; C onsoli, P. M.; Janssen, L. Ferrimagnetism from quantum fluctuations in Kitaev materials. *Phys. Rev. B* **2025**, *112*, 155103.
- (67) C onsoli, P. M.; Janssen, L.; Vojta, M.; Andrade, E. C. Heisenberg-Kitaev model in a magnetic field: $1/S$ expansion. *Phys. Rev. B* **2020**, *102*, 155134.

- (68) Wen, B.; Cen, J.; Kee, H.-Y. Ferrichiral skyrmions with sublattice-resolved chirality in extended Kitaev model in triangular lattice. 2026; <https://arxiv.org/abs/2601.17121>.
- (69) Fert, A.; Reyren, N.; Cros, V. Magnetic skyrmions: advances in physics and potential applications. *Nature Reviews Materials* **2017**, *2*, 17031.
- (70) Seki, S.; Yu, X. Z.; Ishiwata, S.; Tokura, Y. Observation of Skyrmions in a Multiferroic Material. *Science* **2012**, *336*, 198–201.
- (71) Kaiser, U.; Schwarz, A.; Wiesendanger, R. Magnetic exchange force microscopy with atomic resolution. *Nature* **2007**, *446*, 522–525.
- (72) Grenz, J.; Köhler, A.; Schwarz, A.; Wiesendanger, R. Probing the Nano-Skyrmion Lattice on Fe/Ir(111) with Magnetic Exchange Force Microscopy. *Phys. Rev. Lett.* **2017**, *119*, 047205.
- (73) Akazawa, M.; Lee, H.-Y.; Takeda, H.; Fujima, Y.; Tokunaga, Y.; Arima, T.-h.; Han, J. H.; Yamashita, M. Topological thermal Hall effect of magnons in magnetic skyrmion lattice. *Phys. Rev. Res.* **2022**, *4*, 043085.
- (74) Takeda, H.; Kawano, M.; Tamura, K.; Akazawa, M.; Yan, J.; Waki, T.; Nakamura, H.; Sato, K.; Narumi, Y.; Hagiwara, M.; Yamashita, M.; Hotta, C. Magnon thermal Hall effect via emergent SU(3) flux on the antiferromagnetic skyrmion lattice. *Nat. Commun.* **2024**, *15*, 566.
- (75) Kawano, M. Thermal Hall effect and gauge-field picture of magnons in antiferromagnetic skyrmion crystals. *Phys. Rev. B* **2025**, *112*, L060403.
- (76) Lieb, E. H. Flux Phase of the Half-Filled Band. *Phys. Rev. Lett.* **1994**, *73*, 2158–2161.
- (77) Walker, L. R.; Walstedt, R. E. Computer Model of Metallic Spin-Glasses. *Phys. Rev. Lett.* **1977**, *38*, 514–518.
- (78) Berg, B.; Lüscher, M. Definition and statistical distributions of a topological number in the lattice O(3) σ -model. *Nucl. Phys. B* **1981**, *190*, 412–424.
- (79) Díaz, S. A.; Klinovaja, J.; Loss, D. Topological Magnons and Edge States in Antiferromagnetic Skyrmion Crystals. *Phys. Rev. Lett.* **2019**, *122*, 187203.
- (80) Nagaosa, N.; Tokura, Y. Topological properties and dynamics of magnetic skyrmions. *Nat. Nanotechnol.* **2013**, *8*, 899–911.

- (81) Jennewein, D. M. et al. The Sol Supercomputer at Arizona State University. *Practice and Experience in Advanced Research Computing 2023: Computing for the Common Good*. New York, NY, USA, 2023; p 296–301.

**Supplementary Information for “Tuning magnetic
properties of Kitaev materials via an antiferromagnetic
proximity effect: Novel phases and application to
 α -RuCl₃/MnPS₃ bilayer”**

Pedro M. C onsoli,[†] Ezra Day-Roberts,[†] Johannes Knolle,^{‡,¶,§} Antia S. Botana,^{*,†}
and Onur Erten^{*,†}

[†]*Department of Physics, Arizona State University, Tempe, AZ 85287, USA*

[‡]*Munich Center for Quantum Science and Technology (MCQST), Schellingstrasse 4, 80799
Munich, Germany*

[¶]*Technical University of Munich, TUM School of Natural Sciences, Physics Department,
TQM, 85748 Garching, Germany*

[§]*Blackett Laboratory, Imperial College London, London SW7 2AZ, United Kingdom*

E-mail: antia.botana@asu.edu; onur.erten@asu.edu

In this supplementary file, we provide additional details on four aspects discussed in the main text. First, we outline the perturbative calculation we applied to study the effect of a weak staggered field on a Kitaev spin liquid (KSL). Second, we provide additional information on our ED calculations, including data to exemplify how we extracted the phase boundaries in Figs. 2(c) and 2(d) of the main text. Third, we describe the iterative energy-minimization algorithm we applied to obtain classical ground states of Model 1. Fourth, we explain how we computed the topological charges n_{sk}^μ used to characterize the skyrmion crystals uncovered in our classical simulations. And finally, we provide details of the first principles calculations.

Perturbation theory in h around the Kitaev limit

In this section, we show how perturbation theory can be used to infer that a KSL subject to a weak staggered magnetic field develops Majorana Fermi surfaces and antichiral edge modes. This calculation is closely related to the one presented in Kitaev's original paper.¹

We start by separating the full Hamiltonian $\mathcal{H} = \mathcal{H}_0 + \mathcal{V}$ into an unperturbed Kitaev Hamiltonian, \mathcal{H}_0 , and the Zeeman term, \mathcal{V} :

$$\begin{aligned}\mathcal{H}_0 &= \sum_{\gamma} K_{\gamma} \sum_{\langle ij \rangle_{\gamma}} \sigma_i^{\gamma} \sigma_j^{\gamma}, \\ \mathcal{V} &= - \sum_i \mathbf{h}_i \cdot \boldsymbol{\sigma}_i = - \sum_i (-1)^i \sum_{\gamma} h_{\gamma} \sigma_i^{\gamma}.\end{aligned}\tag{S1}$$

As usual, the model is defined on a honeycomb lattice with nearest-neighbor bonds of types $\gamma = x, y, z$ and sublattices A and B . Note that, differently from the main text, we now allow for an arbitrary staggered field $\mathbf{h}_i = (-1)^i \mathbf{h}$. Furthermore, we will work directly with Pauli matrices σ_i^{γ} instead of spin-1/2 operators $S_i^{\gamma} = \hbar \sigma_i^{\gamma} / 2$ for convenience. Unless stated otherwise, we will assume that the Kitaev couplings are isotropic ($K_{\gamma} = K$) for simplicity. However, our results are valid for the entire “ B phase” of the Kitaev model,¹ which is realized when $|K_{\alpha}| \leq |K_{\beta}| + |K_{\gamma}|$ for all permutations (α, β, γ) of (x, y, z) .

Before applying perturbation theory, let us briefly review some of the main ingredients behind Kitaev's exact solution of \mathcal{H}_0 . Following Ref. 1, we can represent each spin-1/2 degree of freedom $\boldsymbol{\sigma}_i$ in terms of four Majorana fermions $\{b_i^x, b_i^y, b_i^z, c_i\}$ obeying the anticommutation relations $\{b_i^{\alpha}, b_j^{\beta}\} = \delta_{ij} \delta_{\alpha\beta}$, $\{b_i^{\alpha}, c_j\} = 0$, and $\{c_i, c_j\} = \delta_{ij}$. With this, the representation $\sigma_i^{\gamma} = ib_i^{\gamma} c_i$ reproduces the appropriate SU(2) spin algebra as long as one imposes the constraint $D_i = b_i^x b_i^y b_i^z c_i = 1$. The unperturbed Hamiltonian then reads

$$\mathcal{H}_0 = -i \sum_{\gamma} K_{\gamma} \sum_{\langle ij \rangle_{\gamma}} \hat{u}_{ij}^{\gamma} c_i c_j,\tag{S2}$$

where $\hat{u}_{ij}^{\gamma} = ib_i^{\gamma} b_j^{\gamma} = -\hat{u}_{ji}^{\gamma}$ is an operator defined for sites i and j that belong to the A and B sublattices, respectively, and are connected by a γ -bond. Since these operators commute with each other and with \mathcal{H}_0 , one can divide the unperturbed Hamiltonian into separate gauge sectors, in which the \hat{u}_{ij}^{γ} operators are replaced by a set of integer eigenvalues $u_{ij}^{\gamma} = \pm 1$.

However, as in any gauge theory, this description is redundant. Two gauge sectors are only inequivalent if they realize different sets of (gauge-invariant) flux eigenvalues $\{w_p\}$, where $w_p = \prod_{(ij) \in p} u_{ij}^{\gamma} = \pm 1$ is given by the product of the u_{ij}^{γ} variables around a given elementary hexagonal plaquette p . It then follows from Lieb's theorem² that the ground state of the system can be obtained by diagonalizing \mathcal{H}_0 within any gauge sector $\{u_{ij}^{\gamma}\}$ that

yields $w_p = +1$ for every p . By doing so, one also finds that the excitations of a KSL with isotropic couplings (or, more generally, of the B phase alluded to above) are gapless Majorana fermions and gapped visons. The latter correspond to fluxes $w_p = -1$, which can only be created in pairs at an energy cost of $\Delta_{2f} \sim |K|$.

Since visons are gapped excitations, the low-energy physics of the full Hamiltonian \mathcal{H} is constrained to the zero-flux subspace \mathcal{L}_0 as long as $h \ll \Delta_{2f}$. If P is a projector onto \mathcal{L}_0 , then the effective low-energy Hamiltonian can be derived via a standard perturbative expansion:

$$\mathcal{H}_{\text{eff}} \equiv \sum_{n=0}^{\infty} \mathcal{H}_{\text{eff}}^{(n)} = \mathcal{H}_0 + P\mathcal{V} \left(\sum_{n=0}^{\infty} R^n \right) P, \quad (\text{S3})$$

where $R = (1 - P)(E - \mathcal{H}_0)^{-1}(1 - P)\mathcal{V}$. Following Ref. 1, we will use the approximation $R \approx -\Delta_{2f}^{-1}(1 - P)\mathcal{V}$, which yields the correct qualitative results for the lowest orders of the perturbation series.

The first-order term $\mathcal{H}_{\text{eff}}^{(1)} = P\mathcal{V}P$ vanishes identically because \mathcal{V} only connects states with different flux configurations. This result can be verified by noting that a single Pauli matrix σ_γ^α commutes with all but one of the \hat{u}_{ij} operators. The exception is the operator \hat{u}_{mn}^γ , for which $\{\sigma_m^\alpha, \hat{u}_{mn}^\gamma\} = 0$. It then follows that if $|\psi_{\{u_{ij}\}}\rangle$ is a state belonging to a gauge sector $\{u_{ij}\}$, $\sigma_m^\alpha |\psi_{\{u_{ij}\}}\rangle$ will be in a gauge sector $\{\tilde{u}_{ij}\}$ which only differs from $\{u_{ij}\}$ in that $\tilde{u}_{mn} = -u_{mn}$. Consequently, $|\psi_{\{u_{ij}\}}\rangle$ and $\sigma_m^\alpha |\psi_{\{u_{ij}\}}\rangle$ have opposite fluxes on the two hexagonal plaquettes joined by the (mn) bond.

The second-order term $\mathcal{H}_{\text{eff}}^{(2)} \approx -\Delta_{2f}^{-1}P\mathcal{V}^2P$ is the first nonvanishing contribution to the perturbation series. One can verify that, apart from shifting the Hamiltonian by a constant, its only effect is to renormalize the Kitaev couplings: $K_\gamma \mapsto \tilde{K}_\gamma = K + (h_\gamma^2/\Delta_{2f})$. Since the correction (h_γ^2/Δ_{2f}) is small compared to K , this renormalization is innocuous: the system remains in the aforementioned B phase, without suffering any qualitative changes.

The first significant change in the low-energy physics of the system comes from

$$\mathcal{H}_{\text{eff}}^{(3)} \approx -\frac{1}{\Delta_{2f}^2} \sum_{i\alpha} \sum_{j\beta} \sum_{k\gamma} (-1)^{i+j+k} h_\alpha h_\beta h_\gamma P \sigma_i^\alpha \sigma_j^\beta \sigma_k^\gamma P. \quad (\text{S4})$$

As in Kitaev's original paper,¹ the projected three-body interaction $P \sigma_i^\alpha \sigma_j^\beta \sigma_k^\gamma P$ can only be nonzero if $\alpha \neq \beta \neq \gamma$. When $(\alpha, \beta, \gamma) = (x, y, z)$, the nonvanishing contributions are due to the spatial configurations (a) and (b) in Fig. S1, both of which conserve all w_p eigenvalues because they flip an *even* number of u_{ij}^γ variables per plaquette. Similar symmetry-related arrangements of (i, j, k) follow for the other combinations of (α, β, γ) .

When expressed in terms of Majorana fermions, third-order contributions of type (a)

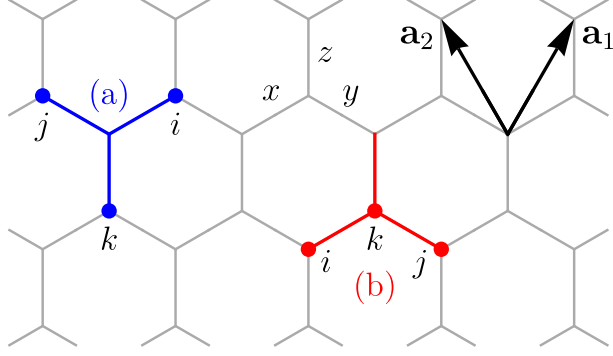


Figure S1: Schematic depicting the sites, i , j , and k , involved in the two types of processes, (a) and (b), which yield a nonzero contribution to the third-order term of the perturbation series. The blue and red lines highlight the bonds whose gauge variables u_{ij}^γ are flipped after the action of the three-body term $\sigma_i^x \sigma_j^y \sigma_k^z$. Also shown are the primitive vectors $\mathbf{a}_1 = (\sqrt{3}, 3)/2$ and $\mathbf{a}_2 = (-\sqrt{3}, 3)/2$ that enter Eqs. (S7) and (S8).

are found to be *quartic* in the itinerant c_i Majoranas. Thus, they do not immediately change the Majorana spectrum and can be neglected. In contrast, type-(b) terms yield $\sigma_i^x \sigma_j^y \sigma_k^z = -i \hat{u}_{ki}^x \hat{u}_{kj}^y c_i c_j D_k$, and therefore map onto a next-nearest-neighbor hopping mediated by the gauge fields.

Hence, by collecting all terms up to third order in Eq. (S3) and choosing a zero-flux gauge with $u_{ij}^\gamma = +1$ on every bond, we obtain the effective Hamiltonian

$$\mathcal{H}_{\text{eff}} = i \left(\sum_{\gamma} \tilde{K}_{\gamma} \sum_{\langle ij \rangle_{\gamma}} c_i c_j + \kappa \sum_{\langle\langle ij \rangle\rangle} v_{ij} c_i c_j \right), \quad (\text{S5})$$

where $\kappa = (h_x h_y h_z) / \Delta_{2f}^2$ and $v_{ij} = \pm 1$ have the sign structure depicted in Fig. 1(b) of the main text. After a Fourier transform, Eq. (S5) becomes

$$\mathcal{H}_{\text{eff}} = \sum_{\mathbf{q}}^{\text{HBZ}} \begin{pmatrix} c_{\mathbf{q}A}^\dagger & c_{\mathbf{q}B}^\dagger \end{pmatrix} \begin{pmatrix} \Delta(\mathbf{q}) & if(\mathbf{q}) \\ -if^*(\mathbf{q}) & \Delta(\mathbf{q}) \end{pmatrix} \begin{pmatrix} c_{\mathbf{q}A} \\ c_{\mathbf{q}B} \end{pmatrix}, \quad (\text{S6})$$

with the sum restricted to half of the Brillouin zone (HBZ). The functions

$$f(\mathbf{q}) = \tilde{K}_x e^{i\mathbf{q} \cdot \mathbf{a}_1} + \tilde{K}_y e^{i\mathbf{q} \cdot \mathbf{a}_2} + \tilde{K}_z, \quad (\text{S7})$$

$$\Delta(\mathbf{q}) = 2\kappa \{ \sin(\mathbf{q} \cdot \mathbf{a}_1) + \sin(\mathbf{q} \cdot \mathbf{a}_2) + \sin[\mathbf{q} \cdot (\mathbf{a}_1 - \mathbf{a}_2)] \}. \quad (\text{S8})$$

are defined in terms of the primitive vectors of the honeycomb lattice, $\mathbf{a}_{1,2} = (\pm\sqrt{3}/2, 3/2)$, shown in Fig. S1. The spectrum of \mathcal{H}_{eff} follows from the diagonalization of the 2×2 matrix

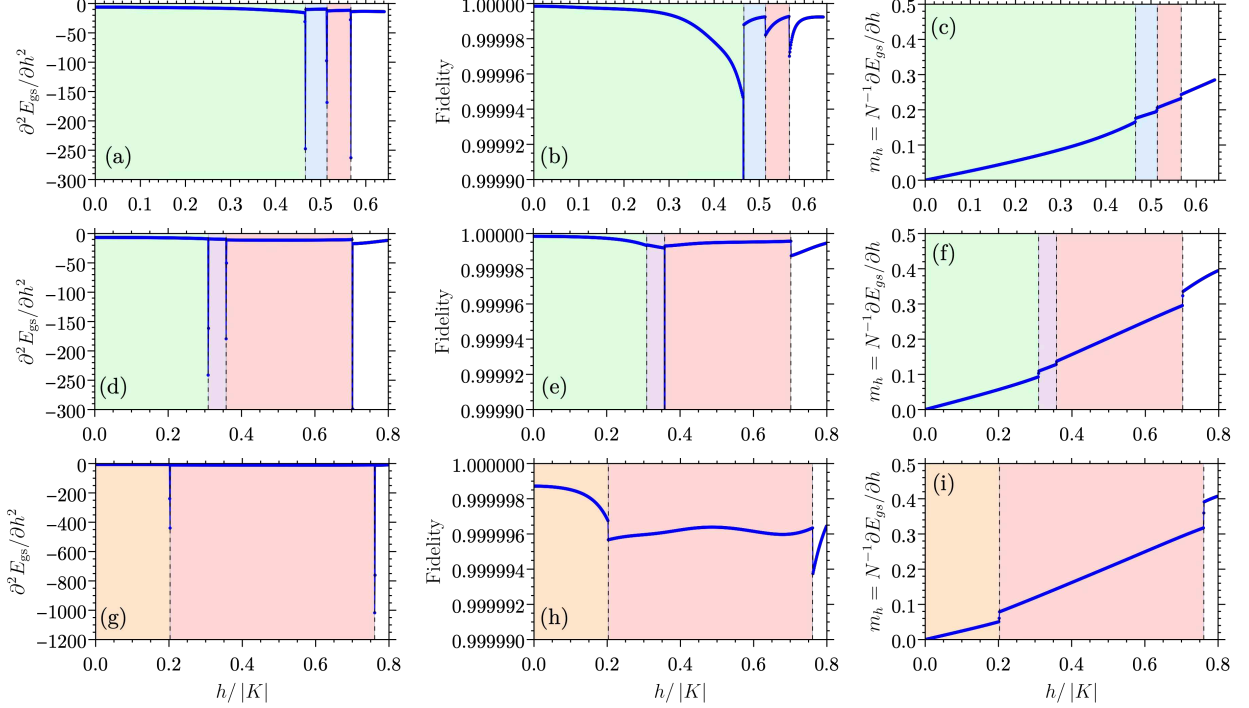


Figure S2: ED results obtained for Model 1 at constant (a-c) $g = 0.02$, (d-h) $g = 0.10$ and (g-i) $g = 0.25$. Different regions in the plots are color-coded to corresponding ground state in Fig. 2(c) in the main text. The first column of plots shows to the second derivative of the ground-state energy with respect to h , $\partial^2 E_{\text{gs}}/\partial h^2$, whereas the second and third columns depict the ground-state fidelity and the staggered magnetization per site. Note that the latter does not saturate in the field-polarized phase because a Néel-type product state where each spin points along the direction of the staggered field is not an eigenstate of the Hamiltonian.

in Eq. (S6):

$$\epsilon_{\pm}(\mathbf{q}) = \Delta(\mathbf{q}) \pm |f(\mathbf{q})|. \quad (\text{S9})$$

Since the renormalized Kitaev couplings $\tilde{K}_{\gamma} = K + h_{\gamma}^2/\Delta_{2f}$ have but a small anisotropy, the function $|f(\mathbf{q})|$ still has zeros at momenta $\pm\mathbf{q}^*$ in the first Brillouin zone.¹ Were it not for $\Delta(\mathbf{q})$, this would give rise to a pair of Dirac cones at zero energy. However, since $\Delta(-\mathbf{q}) = -\Delta(\mathbf{q})$, the Dirac cones are now subject to opposite energy shifts $\pm|\Delta(\mathbf{q}^*)|$, as illustrated in Fig. 1(b) in the main text. When $\mathbf{h} \parallel [111]$ as in the main text, we find that $\mathbf{q}^* = K = 4\pi/(3\sqrt{3})\hat{\mathbf{x}}$ and the splitting $|\Delta(\mathbf{q}^*)| = 3\sqrt{3}\kappa$.

Additional information on exact diagonalization

As mentioned in the main text, when performing our ED calculations, we exploited the translational symmetry of the 24-site cluster to decompose the Hamiltonian into sectors of different momenta \mathbf{k} . If T_1 and T_2 denote the operators that implement translations

by the vectors $\mathbf{a}_1 = (\sqrt{3}, 3)/2$ and $\mathbf{a}_2 = (0, 3)$ shown in Fig. 1(a) of the main text, then each momentum sector is composed of states $|\phi\rangle$ satisfying $T_n |\phi\rangle = e^{i\mathbf{k}\cdot\mathbf{a}_n} |\phi\rangle$ for a different momentum $\mathbf{k} = \frac{\pi}{3\sqrt{3}}(2n_1 - 3n_2, \sqrt{3}n_2)$, with $n_1, n_2 \in \mathbb{Z}$.

In Fig. S2, we present additional ED data to illustrate how the phase boundaries in Figs. 2(c) and 2(d) of the main text were extracted. Because of finite-size effects, continuous phase transitions tend to be associated with *smooth* peaks in the second derivatives of the ground-state energy and the fidelity. By contrast, first-order transitions lead to sharp features that also manifest in observables such as the staggered magnetization per site

$$m_h = \frac{1}{Nh} \sum_i \mathbf{h}_i \cdot \langle \mathbf{S}_i \rangle, \quad (\text{S10})$$

depicted in the right panels.

Iterative minimization

Our classical simulations, whose results were discussed in the main text, made use of an iterative energy-minimization method related to the algorithm presented in Ref. 3. Our algorithm is composed of the following steps:

1. Given a finite-size cluster Λ , initialize the unit vectors $\{\mathbf{S}_i\}$ in a random configuration.
2. Compute the set of local fields

$$H_i^\alpha = h_i^\alpha - \sum_{j,\beta} J_{ij}^{\alpha\beta} S_j^\beta. \quad (\text{S11})$$

Here, $J_{ij}^{\alpha\beta}$ is a matrix that includes all interactions between the spins at sites i and j . It is defined by rewriting the Hamiltonian from Eqs. (1) and (2) in the main text as $\mathcal{H} = \frac{1}{2} \sum_{i,j} \sum_{\alpha,\beta} S_i^\alpha J_{ij}^{\alpha\beta} S_j^\beta - \sum_i \mathbf{h}_i \cdot \mathbf{S}_i$.

3. Generate a new spin configuration $\{\mathbf{S}'_i\}$ defined by

$$\mathbf{S}'_i = \frac{1}{\mathcal{N}_i} \left[r_i \hat{\mathbf{H}}_i + (1 - r_i) \mathbf{S}_i \right], \quad (\text{S12})$$

where $\hat{\mathbf{H}}_i = \mathbf{H}_i/|\mathbf{H}_i|$, r_i is a random number uniformly sampled from an interval $[r_{\min}, r_{\max}]$ with $0 \leq r_{\min} < r_{\max} \leq 1$, and \mathcal{N}_i is a normalization constant chosen to ensure that $|\mathbf{S}'_i| = 1$.

4. Compute the deviations $\varepsilon_i = |\mathbf{S}_i - \mathbf{S}'_i|$ and substitute $\{\mathbf{S}'_i\} \rightarrow \{\mathbf{S}_i\}$.

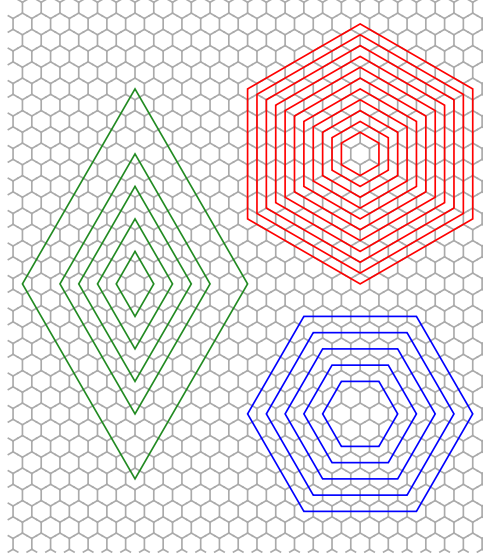


Figure S3: Different clusters used in our iterative minimization study. The smallest blue cluster corresponds to the 24-site cluster utilized in our ED simulations.

5. Iterate steps 2-4 until the maximum deviation is less than a prescribed tolerance Δ , i.e., $\max(\varepsilon_i) \leq \Delta$.
6. Repeat steps 1-5 for N_{init} different initial configurations and store the state $\{\mathbf{S}_i^\Lambda\}$ with the lowest energy.

In our simulations, we used simulation parameters $r_{\text{min}} = 0.1$, $r_{\text{max}} = 0.3$, $\Delta = 10^{-10}$, and $N_{\text{init}} = 10^3$. Moreover, for each set of model parameters g and h , we applied the iterative method to the 21 clusters depicted in Fig. S3, all of which were subject to periodic boundary conditions. In the end, we selected the state $\{\mathbf{S}_i^\Lambda\}$ with the lowest energy per spin.

Computation of topological charges

The topological charges n_{sk}^μ ($\mu = A, B$) mentioned in the main text are computed as^{4,5}

$$n_{\text{sk}}^\mu = \frac{1}{2\pi} \sum_{\Delta, \nabla} \arctan \left[\frac{\mathbf{S}_i \cdot (\mathbf{S}_j \times \mathbf{S}_k)}{1 + \mathbf{S}_i \cdot \mathbf{S}_j + \mathbf{S}_i \cdot \mathbf{S}_k + \mathbf{S}_j \cdot \mathbf{S}_k} \right], \quad (\text{S13})$$

where the sum runs over all elementary plaquettes (Δ or ∇) of sublattice μ in the magnetic unit cell. For any given plaquette, the sites (i, j, k) are ordered in the same way, e.g., anti-clockwise. Moreover, \arctan refers to the principal branch of the arctangent function, whose image is $(-\pi/2, \pi/2]$. As a discretized version of the usual skyrmion number,⁶ Eq. (S13) is an integer that counts the number of times the spin configuration wraps the unit sphere.

Density functional theory calculation

To obtain a characteristic coupling scale for the real material bilayer, we calculate the energy difference between a state with ferromagnetic layers coupled ferromagnetically and the same ferromagnetic layers coupled anti-ferromagnetically from density functional theory simulations. For these calculations, we used the VASP code and the projector-augmented-wave (PAW) approach^{7,8} along with the PBE pseudopotential.⁹ A $8 \times 4 \times 1$ Γ centered k-point grid was used for monolayer calculations with a 600 eV energy cutoff. All calculations were done including spin-orbit coupling.¹⁰

A bilayer was constructed from the experimental C2/m bulk structures for RuCl_3 ¹¹ and MnPS_3 ¹² including ~ 20 Å of vacuum. The lattice constants were taken from MnPS_3 to mimic a monolayer of RuCl_3 atop an MnPS_3 bulk. This setup would provide the most uniform field experienced by the RuCl_3 . The atomic coordinates were then relaxed under a fully ferromagnetic order. Finally, the energies in a fully ferromagnetic state and a state consisting of ferromagnetic layers coupled anti-ferromagnetically were computed to determine the energy difference per Ru atom.

References

- (1) Kitaev, A. Anyons in an exactly solved model and beyond. *Ann. Phys.* **2006**, *321*, 2–111.
- (2) Lieb, E. H. Flux Phase of the Half-Filled Band. *Phys. Rev. Lett.* **1994**, *73*, 2158–2161.
- (3) Walker, L. R.; Walstedt, R. E. Computer Model of Metallic Spin-Glasses. *Phys. Rev. Lett.* **1977**, *38*, 514–518.
- (4) Berg, B.; Lüscher, M. Definition and statistical distributions of a topological number in the lattice $O(3)$ σ -model. *Nucl. Phys. B* **1981**, *190*, 412–424.
- (5) Díaz, S. A.; Klinovaja, J.; Loss, D. Topological Magnons and Edge States in Antiferromagnetic Skyrmion Crystals. *Phys. Rev. Lett.* **2019**, *122*, 187203.
- (6) Nagaosa, N.; Tokura, Y. Topological properties and dynamics of magnetic skyrmions. *Nat. Nanotechnol.* **2013**, *8*, 899–911.
- (7) Kresse, G.; Furthmüller, J. Efficient iterative schemes for ab initio total-energy calculations using a plane-wave basis set. *Phys. Rev. B* **1996**, *54*, 11169–11186.
- (8) Kresse, G.; Joubert, D. From ultrasoft pseudopotentials to the projector augmented-wave method. *Phys. Rev. B* **1999**, *59*, 1758–1775.

- (9) Perdew, J. P.; Burke, K.; Ernzerhof, M. Generalized Gradient Approximation Made Simple. *Phys. Rev. Lett.* **1996**, *77*, 3865–3868.
- (10) Kim, H.-S.; Kee, H.-Y. Crystal structure and magnetism in α – RuCl₃: An ab initio study. *Phys. Rev. B* **2016**, *93*, 155143.
- (11) Cao, H. B.; Banerjee, A.; Yan, J.-Q.; Bridges, C. A.; Lumsden, M. D.; Mandrus, D. G.; Tennant, D. A.; Chakoumakos, B. C.; Nagler, S. E. Low-temperature crystal and magnetic structure of α -RuCl₃. *Phys. Rev. B* **2016**, *93*, 134423.
- (12) Ouvrard, G.; Brec, R.; Rouxel, J. Structural determination of some MPS3 layered phases (M = Mn, Fe, Co, Ni and Cd). *Materials Research Bulletin* **1985**, *20*, 1181–1189.